Research Square

Preprints are preliminary reports that have not undergone peer review.
They should not be considered conclusive, used to inform clinical practice,
or referenced by the media as validated information.

Laser-Structured Copper Surfaces for Paste-Free Direct Cu/Cu Joining

Cheng Zhang

cheng.zhang_jhu@hotmail.com

Chemnitz University of Technology: Technische Universitat Chemnitz https://orcid.org/0009-0009-7267-9300

Matthias Tuerpe

Dresden University of Technology: Technische Universitat Dresden

Philipp Steinert

Chemnitz University of Technology: Technische Universitat Chemnitz

Andreas Schubert

Chemnitz University of Technology: Technische Universitat Chemnitz

Research Article

Keywords: laser surface structuring, direct Cu/Cu joining, paste-free joining, surface topography, fracture analysis, power electronics packaging

Posted Date: November 6th, 2026

DOI: https://doi.org/10.21203/rs.3.rs-11156221/v1

License: This work is licensed under a Creative Commons Attribution 4.0 International License.
Read Full License

Laser-Structured Copper Surfaces for Paste-Free Direct Cu/Cu Joining

Cheng Zhang[1, 2, *], Matthias Tuerpe[2], Philipp Steinert[3] and Andreas Schubert[3]
[1]Institute of Materials Science and Engineering, Chemnitz University of Technology, Chemnitz, Germany
[2]Formerly with Corporate Research, Functional Surface Technology, MAHLE International GmbH, Stuttgart, Germany
[3]Micromanufacturing Technology, Institute for Machine Tools and Production Processes, Chemnitz University of Technology, Chemnitz, Germany

*Corresponding author: cheng.zhang_jhu@hotmail.com

Abstract

The increasing thermal and power-density requirements of modern electronic systems create a growing demand for joining technologies that provide high electrical and thermal conductivity, sufficient mechanical stability, and reduced process complexity. This study investigates a paste-free approach for direct Cu/Cu joining using laser-structured copper surfaces. A kinematic surface simulation was used to identify laser parameter combinations that generate pronounced microstructured topographies. Two structure variants with different lateral feature sizes and surface-enlargement factors were subsequently produced and joined under heat and pressure without a filler metal, sintering paste, or permanent intermediate layer. The resulting surfaces and joints were characterized by optical microscopy, scanning electron microscopy, laser scanning microscopy, cross-sectional analysis, fracture-surface examination, and preliminary adapted die-shear testing. Apparent shear strengths of approximately 16 and 35 MPa were obtained for structure variants I and II, respectively. Variant II exhibited finer and more densely distributed features, a larger surface-enlargement factor, and a more continuous interfacial contact morphology. The results indicate that laser-generated microstructures can support paste-free direct Cu/Cu joining and that the lateral distribution of the surface features is an important factor in joint formation.

Keywords: laser surface structuring; direct Cu/Cu joining; paste-free joining; surface topography; fracture analysis; power electronics packaging

1. Introduction

The increasing use of wide-bandgap semiconductors, particularly silicon carbide (SiC), enables power-electronic devices to operate at higher temperatures, voltages, switching frequencies, and power densities. To fully exploit these advantages, die-attach and joining technologies must provide high thermal conductivity, low electrical resistance, sufficient mechanical strength, and long-term reliability under thermal and power-cycling conditions [1–3]. Conventional solder joints are still widely used in electronic packaging; however, their performance at elevated temperatures can be limited by creep deformation, microstructural coarsening, intermetallic-compound growth, and thermomechanical fatigue [1–4].

Silver sintering is one of the most established alternatives for high-temperature power-electronic packaging. Sintered silver joints combine relatively low processing temperatures with high thermal and electrical conductivity and good thermal stability [1,2,5–8]. However, conventional silver-sintering processes generally require a separately applied paste, film, or preform. Process steps such as printing, drying, decomposition of organic constituents, gas removal, and control of the joining-layer thickness increase process complexity and may

contribute to residual porosity and local inhomogeneity [5–8]. In addition, the comparatively high cost of silver has increased interest in copper-based joining technologies [2,9].

Copper is attractive because of its high thermal and electrical conductivity, broad availability, and lower material cost. Considerable progress has been made in low-temperature copper sinter joining using micro- and nanoparticles, reducing agents, protective coatings, composite particles, and controlled atmospheres [9–12]. Nevertheless, most copper-sintering processes still require a separately deposited paste or film. Copper oxidation also remains a major challenge because surface oxides can restrict direct metallic contact, atomic diffusion, and neck formation during joining [9–13].

A direct and paste-free Cu/Cu joining process could simplify the manufacturing chain and avoid process steps and defects associated with binder decomposition, paste shrinkage, and residual porosity. Direct Cu/Cu bonding has already been investigated for thermocompression bonding, wafer-level packaging, hybrid bonding, and three-dimensional integration [14–18]. These approaches commonly require highly flat and clean surfaces, surface activation, oxidation protection, controlled atmospheres, or comparatively high joining temperatures and pressures [14–18].

A key challenge in direct Cu/Cu joining is the limited real contact area between the joining partners. Even nominally flat surfaces initially contact each other only at individual asperities. Native copper oxides and surface contamination can further reduce direct metal-to-metal contact [14,15,18]. During thermocompression bonding, the applied pressure deforms surface asperities and increases the real contact area, while elevated temperature facilitates plastic deformation and promotes the formation of metallic contact across the interface [14–18].

Defined surface structuring offers a possible route to modify these contact conditions. One example is the so-called NanoWired connection technology, in which dense arrays of metallic nanowires are produced on the joining surfaces by an electrochemical deposition process [19]. During joining, opposing nanowire structures are brought into contact under pressure and, depending on the process conditions, elevated temperature. The nanowire arrays provide a large number of local contact points and can form solder-free metallic interconnections. Cu nanowire interconnects have been demonstrated under ambient conditions, with the resulting mechanical strength depending strongly on nanowire diameter, bonding pressure, and temperature [19]. This approach has therefore been investigated as an alternative to conventional soldering and particle-based silver or copper sintering.

These findings raise the question of whether the local pressure concentration achieved by nanowire arrays can also be realized using laser-generated microstructures. Defined columnar or cone-like features with small initial contact areas may concentrate the applied load and generate locally high stresses during compression. This may promote plastic deformation, locally disturb surface oxides, and increase the real metallic contact area. The interaction between opposing structures may also support mechanical interaction and load transfer across the interface [20–22].

Laser surface structuring is well suited for producing defined topographies because it is contact-free, tool-free, locally adaptable, and digitally controlled [20–23]. Depending on the laser parameters and scanning strategy, grooves, cavities, ridges, pins, and cone-like features can be generated. Their geometry is influenced by laser power, pulse duration, pulse overlap, scanning velocity, hatch spacing, and the number of processing passes [20–23].

Previous studies have shown that laser-generated structures can improve the strength of adhesive and polymer–metal interfaces by increasing the developed surface area and

promoting mechanical interlocking [20–22]. Laser processing can also modify the roughness, oxide condition, surface chemistry, and wettability of copper [23–25]. Although these joining systems differ from direct metallic Cu/Cu joining, they demonstrate that laser-generated topographies can be used to influence interfacial contact and load transfer.

Despite extensive research on copper sintering, planar Cu/Cu bonding, and laser-structured interfaces, relatively little attention has been paid to defined laser-generated copper topographies for paste-free direct Cu/Cu joining. Existing Cu/Cu studies mainly focus on planar surfaces, oxidation protection, grain-structure control, and surface activation [14–18], whereas investigations of laser-structured interfaces predominantly address adhesive bonding, polymer–metal joining, wettability, and ultrasonic welding [20–25]. Consequently, the relationship between laser-generated surface morphology, local contact formation, mechanical response, and fracture behavior in paste-free Cu/Cu joining remains insufficiently understood.

The present study investigates two laser-structured copper surfaces for paste-free direct Cu/Cu joining. The work combines kinematic process simulation, laser surface structuring, topographical characterization, thermomechanical joining, preliminary adapted die-shear testing, cross-sectional analysis, and fracture-surface examination. The primary objective is to identify suitable laser-generated microstructures and corresponding process parameter ranges and to evaluate their joining capability. Particular attention is given to the influence of surface morphology on local contact formation, apparent shear strength, interfacial morphology, and fracture behavior.

2. Materials and Methods

2.1 Kinematic Process Simulation

In laser surface structuring, the resulting topography is determined by the interaction between the processing parameters, the scanning strategy, and the superposition of successive material-removal events. In addition to pulse and line spacing, parameters such as scan direction, number of passes, and the relative orientation of successive scan paths can significantly influence the resulting surface morphology and roughness [26].

Kinematic surface simulation is a geometric-numerical approach for predicting manufacturing-induced surface topographies. The method describes the surface microgeometry on the basis of the relative motion between the effective process zone and the workpiece. The main model components are the geometric representation of the effective tool or process zone, the process kinematics, and a discrete representation of the workpiece surface. The resulting topography is generated by the successive geometric interaction between the effective tool geometry and the workpiece. This general principle has been applied to various cutting, machining, and ablation processes [27–29].

For the kinematic simulation of ablation processes, a single ablation geometry (crater)—generated experimentally and topographically measured—is interpreted as an equivalent tool geometry and used as a geometric ablation tool. The total surface is then generated through the step-by-step Boolean interaction of this single ablation geometry with the digitized workpiece along the specified pulse positions. When an experimentally measured single-pulse ablation is used, various complex processes of laser-material interaction are already implicitly contained within the tool geometry used. These include the melting and vaporization processes resulting from laser-material interaction, as well as material deposits at the crater rim. However, these processes are characterized by stochastic factors (melt dynamics, material inhomogeneities, and variations or accuracies of the coordinate systems), which influence the degree of roughness and can be accounted for using additional models,

e.g., by the integration of fluence dependencies [30]. An experimentally determined ablation crater is, in principle, representative only of the specific combination of material, wavelength, pulse duration, focal geometry, fluence or pulse energy, and, if applicable, environmental conditions. By coupling a kinematic simulation with multiphysical simulation methods, the relationships between laser and material parameters and the characteristics of single-pulse ablation can be fully accounted for within the framework of numerical modeling [31].

As part of this work, a kinematic simulation model was developed that incorporates stochastic components in the process using a model-based approach, in order to quantify the relationship between machining parameters and surface structure and roughness, and, based on this, to select suitable process parameter ranges, particularly for pulse and line spacing and the number of passes.

2.2 Laser Surface Structuring

The laser structuring process was conducted under atmospheric conditions by a Nd:YVO_4 nanosecond laser system (specifications: wavelength = 532 nm, pulse duration = 10 ns, max. average power = 13 W, beam shape gaussian, beam quality $M^2 < 1.3$, focus diameter = 15 µm, manufacturer: Spectra Physics®, Santa Clara, CA, USA) with a telecentric F-Theta lens with a focal length = 80 mm [20].

According to the selected and simulated strategy, multiple, line-wise scanning of the copper surface area with varying frequency and thus energy of single pulses was performed for the realization of the surface microstructures. The machining strategy with the relevant parameters is shown in Figure 1.

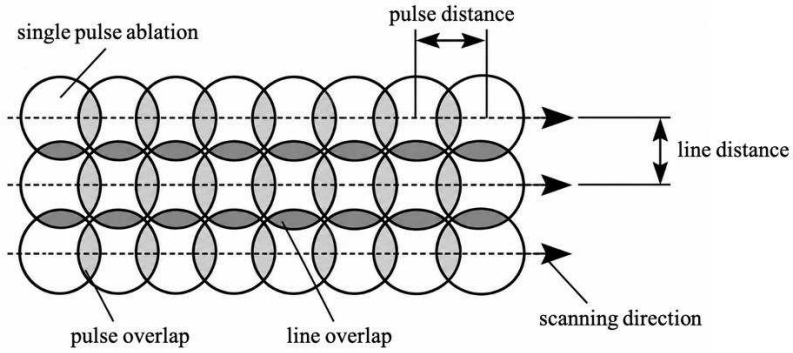


Fig.1 Machining strategy for laser surface structuring

With support of the surface simulations, it was the aim to obtain pin-like profile elements distributed in a grid, resulting in the highest possible surface roughness value *Sa*. For simplification, pulse and line distance were set equal in each case. Table 1 shows selected laser parameters and calculated energy-related quantities.

Tab.1 Laser-processing parameters used for the generation and simulation of the copper surface structures.

Laser Parameter	Value / Range	Unit
Pulse frequency *f* (pulse energy, calc.)	100 (130) … 200 (65)	kHz (µJ)
Number of passes *n*	10 … 50	-
Pulse / line distance *pd*	5 … 50	µm

2.3 Copper Substrates

Copper shear specimens made of Cu-OF (CW008A) with a thickness of 3 mm were used for the joining experiments, as shown in Figure 2. The lower copper substrate had dimensions of 40 mm × 22 mm. A square copper matrix with dimensions of 8 mm × 8 mm was positioned in the central joining area, resulting in a nominal joining area of 64 mm^2.

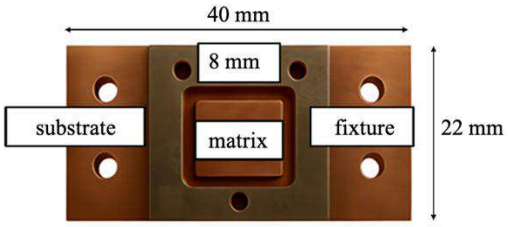


Fig.2 Geometry of the copper shear specimen with an 8 mm × 8 mm copper matrix and the mechanical positioning fixture.

The matrix was aligned relative to the substrate using a metallic fixture. The fixture contained a square opening corresponding to the dimensions of the matrix and ensured reproducible positioning during assembly and joining. Additional holes in the copper substrate and fixture were used for fixation and alignment.

2.4 Characterization of Laser-Structured Surfaces

After laser processing, the copper surfaces were characterized prior to joining in order to document the generated surface morphology and to assess the reproducibility of the laser-generated structures. The characterization combined optical microscopy, scanning electron microscopy (SEM), and laser scanning microscopy (LSM), providing both qualitative morphological information and quantitative surface-topography data.

Optical microscopy was first used to obtain an overview of the complete laser-processed area. The examinations were carried out using an Axio Imager.M2m microscope (Carl Zeiss, Germany). The images were evaluated with respect to the uniformity, continuity, and overall distribution of the laser-generated structures. Representative regions were subsequently selected for higher-resolution analysis.

The detailed surface morphology was investigated by SEM using a Sigma 360 VP (Carl Zeiss, Germany). Particular attention was paid to the shape, size, spacing, and lateral distribution of the laser-generated features, as these characteristics determine the initial contact geometry between the opposing copper surfaces during joining.

LSM was used for the three-dimensional and quantitative characterization of the surface topography. Representative surface maps were obtained from defined regions of the structured joining areas. The evaluation included the areal surface-topography parameters *Sa* and *Sz*, as well as the surface-enlargement factor. Here, *Sa* denotes the arithmetical mean height, whereas *Sz* denotes the maximum height of the surface. The surface-enlargement factor was determined under the applied measurement and data-processing conditions and therefore depends on the evaluated area, filtering, and corresponding processing settings.

The results obtained by optical microscopy, SEM, and LSM were evaluated collectively to describe the laser-structured surfaces before joining. These data were subsequently used to relate the surface morphology and topography to the observed interfacial contact formation, fracture morphology, and mechanical response of the Cu/Cu joints.

2.5 Paste-free Cu/Cu Joining Process

The paste-free Cu/Cu joining process is illustrated in Figure 3.

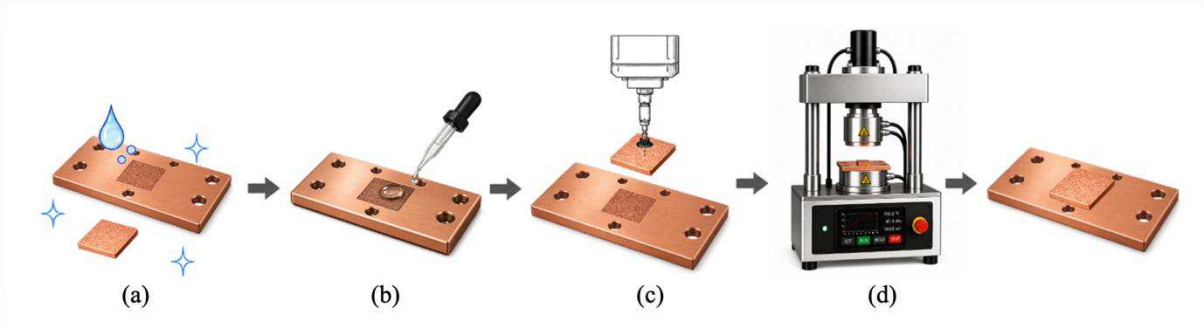


Fig.3 Schematic workflow of the paste-free Cu/Cu joining process: (a) cleaning of the copper surfaces; (b) application of the copper-surface activator; (c) positioning of the Cu matrix on the laser-structured substrate; and (d) thermomechanical joining under heat and pressure.

Before joining, the laser-structured copper substrate and the copper matrix were cleaned with ethanol to remove loose particles and organic surface contamination and were subsequently dried under ambient conditions. A small amount of a copper-surface activator supplied by NanoWired GmbH, Germany, was then applied locally to the structured joining areas. According to the supplier, the activator is intended to reduce the influence of the native copper oxide layer and to support the formation of direct metallic contact during thermomechanical joining. The activator was not used as a filler material and was not intended to form a permanent intermediate joining layer. The detailed chemical composition of the activator was not disclosed by the supplier.

The copper matrix was positioned on the corresponding structured region of the substrate. The structured surfaces of the two copper components were arranged face-to-face, resulting in a nominal joining area of 64 mm².

The assembled specimens were subsequently joined at a temperature of 250 °C, a nominal pressure of 20 MPa, and a holding time of 5 min. After joining, the specimens were prepared for mechanical testing, cross-sectional characterization, and fracture-surface analysis.

2.6 Mechanical Testing and Metallographic Analysis

The mechanical response of the paste-free Cu/Cu joints was evaluated by adapted die-shear testing using a custom shearing fixture mounted in a universal testing machine (ZwickRoell Z010, ZwickRoell GmbH & Co. KG, Germany). As shown in Figure 4, the specimen was fixed in a rigid metallic holder, and the shear tool was positioned close to the lower edge of the 8 mm × 8 mm copper matrix. The load was applied parallel to the joining interface until the peak shear force was reached and a subsequent force drop was observed. The apparent shear strength was calculated from the measured peak force and the nominal joining area of 64 mm².

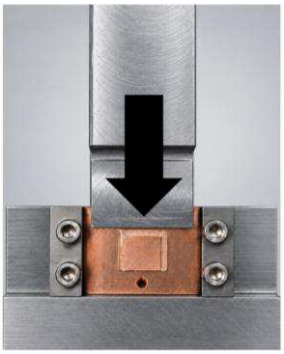


Fig.4 Experimental setup for the adapted die-shear testing of the paste-free Cu/Cu joints, shown in front view.

After shear testing, the corresponding fracture surfaces were examined by SEM. In addition, cross-sections of selected bonded specimens were prepared and analyzed by optical microscopy and SEM. The metallographic analysis focused on local bonded and unbonded regions, deformation of the laser-generated structures, material transfer, interfacial gaps, and indications of mechanical interaction between the joining partners. The metallographic observations were subsequently compared with the measured apparent shear strengths to assess the relationship between surface morphology, joint formation, and failure behavior.

3. Results and Discussion

3.1. Simulation of Surface Topography

As part of the simulation studies, a kinematic surface model was developed based on the approach described in [31] and implemented in MATLAB. The model enables the superposition of individual experimentally measured ablation geometries. Single-pulse ablation craters were measured by confocal microscopy using a Keyence VK9700 laser microscope (408 nm, 50× long-distance objective) and subsequently digitized. To account for stochastic process deviations, spatial displacements caused by positioning errors and random angular rotations of the individual pulse-ablation geometries were introduced. In addition, a random offset between adjacent scan lines caused by the scanner control was considered.

With regard to the machining strategy, a two-dimensional, deterministic structuring approach was selected. Based on the focal diameter, it was expected that surface roughness would tend to be low for both very small and very large pulse and line spacings, and that it would tend to be high for pulse and line spacings in the range of the focal diameter. The resulting roughness was determined using the roughness parameters *Sa* and *Sz* in accordance with ISO 25178 [32] and evaluated as a basis for comparison.

For the simulations, pulse repetition frequencies of 100 kHz and 200 kHz were selected with different pulse and line spacings as well as the number of passes, as specified in Table 1. By the representation of a dexel-based height model, a smooth initial surface (250 µm × 250 µm) with a pixel spacing of 1 µm was defined as the workpiece. For the evaluation and visualization of the results, the mean value of the roughness *Sa* was determined from three simulation runs with constant number of passes $n = 10$. Figure 5 shows the progression of the surface roughness Sa and Sz for different pulse repetition frequencies $f = 100$ kHz and $f = 200$ kHz. For a detailed view, some selected surfaces specified in Figure 5 are plotted in Figure 6 in the form of surface sections of 120 µm × 100 µm.

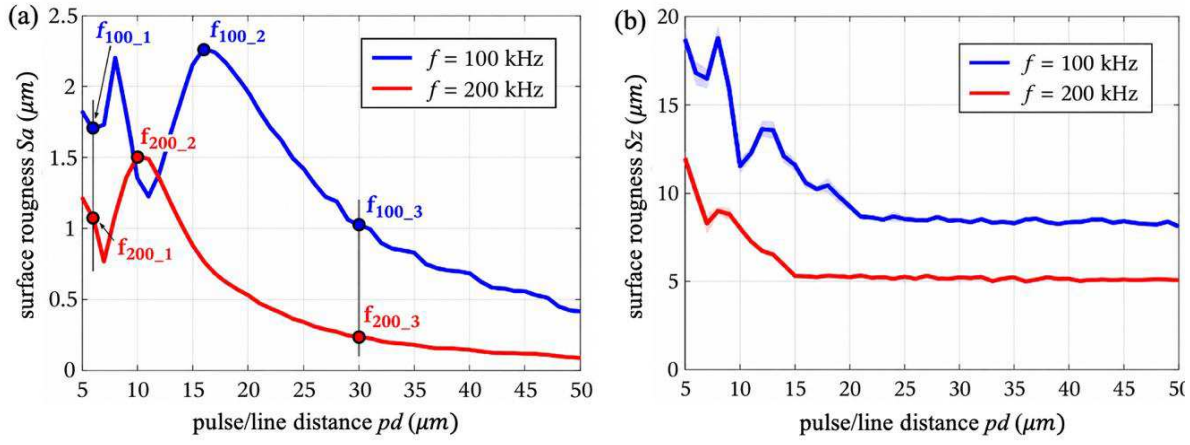


Fig.5 Calculated areal roughness parameters as a function of pulse/line spacing for pulse repetition frequencies of 100 and 200 kHz: (a) *Sa*; (b) *Sz*.

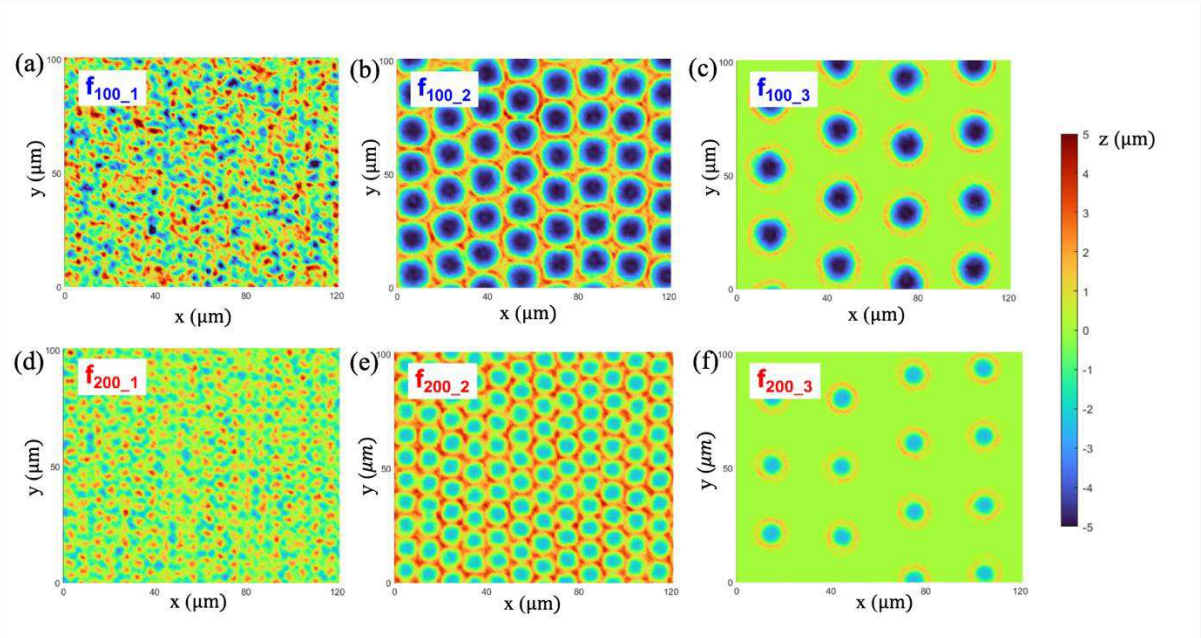


Fig.6 Representative simulated surface topographies for n = 10 passes at selected pulse/line spacings: (a) f = 100 kHz, pd = 5 µm; (b) f = 100 kHz, pd = 16 µm; (c) f = 100 kHz, pd = 30 µm; (d) f = 200 kHz, pd = 5 µm; (e) f = 200 kHz, pd = 10 µm; and (f) f = 200 kHz, pd = 30 µm.

As expected, it was found that Sa increases as the pulse/line spacing ranges within the focus diameter. This represents the regular arrangement of individual pulse ablations characteristic of deterministic structuring (see Figure 6, *f*100_2 and *f*200_2). In the case of the higher frequency some variations have been observed in the range of lower pulse/line spacing. This might be caused by interference effects, whereby the structure heights increase or decrease depending on the pulse distance to ablation diameter ratio.

It was also found that the maximum roughness Sa occurs at $pd \approx 16$ µm for f = 100 kHz and at $pd \approx 10$ µm for f = 200 kHz and that the value increases linearly with the number of passes. Interestingly, the conducted geometric simulation shows that the roughness value *Sz* tends to increase as the pulse-to-line spacing decreases. This may be caused by the random formation of individual peaks or valleys in the surface profile (cmp Figure 6, *f*100_1). However, the observed roughness values are overestimated by tendency in the simulation due to the simple, additive superposition of the individual pulses, resulting in Sa = 5.5 µm and Sz = 23.6 µm for f = 100 kHz, pd = 16 µm, n = 25 as well as Sa = 7.2 µm and Sz = 33.7 µm for f = 200 kHz, pd = 10 µm, n = 50 (cmp. Section 3.2, Table 2). It is assumed that these deviations to the experiment occur due to the changed conditions of the energy input, e.g. changed reflection, during multiple impacts of the laser pulses.

Based on the results of the simulation studies, two sets of process parameters were selected for each of the two frequencies (variant I: f = 100 kHz, pd = 16 µm, n = 25; variant II: f = 200 kHz, pd = 10 µm, n = 50), which exhibit sufficiently large *Sa* roughness values and differ in terms of the scaling of the structural elements due to the different pulse energies. Accordingly, at lower frequencies, larger structures form due to the higher individual pulse energy (variant I), while a higher frequency leads to finer structural elements (variant II) due to the lower individual pulse energies. The following section presents a more detailed metrological analysis of the resulting surface structures.

3.2. Morphology of Laserstructured Copper Surfaces

The morphology of the two selected laser-structured copper surfaces was characterized by LSM and SEM. Representative SEM images at different magnifications are shown in Figure 7, while the corresponding topographical parameters are summarized in Table 2.

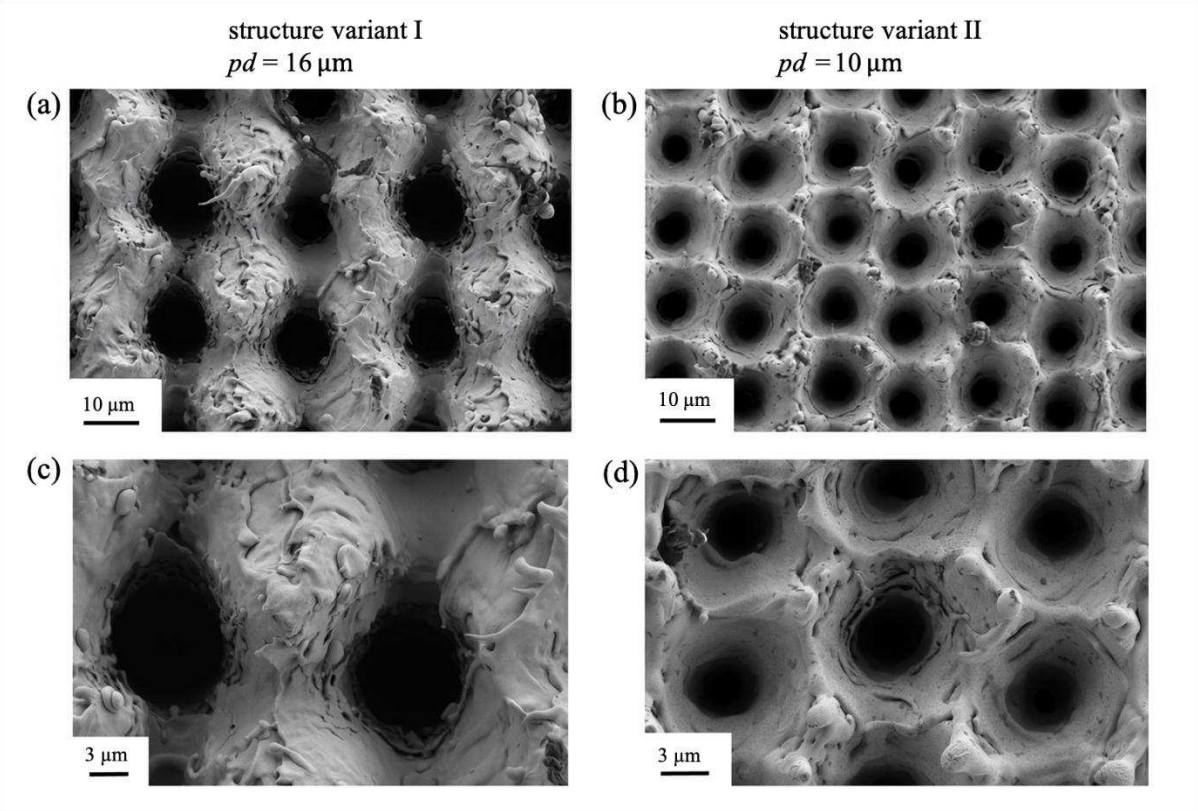


Fig.7 SEM images of the two selected laser-structured copper surfaces at different magnifications: (a,c) structure variant I and (b,d) structure variant II. Structure variant I exhibits larger and more widely spaced features, whereas structure variant II shows a finer and more densely distributed morphology.

The two structure variants exhibited clearly different surface geometries. Structure variant I was characterized by a periodic arrangement of comparatively large cone-like features with pronounced material accumulation around their edges. Structure variant II also exhibited a periodic cone-like morphology; however, the individual features were smaller and more densely distributed, resulting in a finer and more homogeneous surface pattern.

Tab.2 Areal surface-topography parameters of the selected laser-structured copper surfaces. *Sa* denotes the arithmetical mean height and *Sz* the maximum height of the surface. The surface-enlargement factor depends on the applied measurement and evaluation conditions, including the evaluated area and filtering. Values are given as mean ± standard deviation ($n = 3$).

Structure variant	*Sa* (µm)	*Sz* (µm)	Surface enlargement factor
I	3.7 ± 0.3	27.3 ± 0.6	6.1 ± 1.3
II	2.3 ± 0.2	24.4 ± 3.4	8.0 ± 0.5

The quantitative LSM results confirmed the morphological differences between the two structure variants. Structure variant I exhibited higher areal roughness values, with $Sa = 3.7 \pm 0.3$ µm and $Sz = 27.3 \pm 0.6$ µm, whereas variant II showed lower values of $Sa = 2.3 \pm 0.2$ µm and $Sz = 24.4 \pm 3.4$ µm. In contrast, variant II exhibited a higher surface-enlargement factor of 8.0 ± 0.5, compared with 6.1 ± 1.3 for variant I. This indicates that the larger developed surface of variant II was mainly associated with the finer and more densely distributed lateral surface features rather than with a larger areal roughness amplitude.

Compared with the simulated values presented in Section 3.1, differences in the absolute *Sa* and *Sz* values were observed. Nevertheless, the experimentally generated surfaces qualitatively confirmed the different structural scales predicted by the simulation. Variant I exhibited larger and more widely spaced features, whereas variant II showed a finer and more densely distributed morphology with a higher surface-enlargement factor.

Overall, both variants exhibited pronounced periodic laser-generated microstructures. The differences in feature size, lateral density, areal roughness, and surface enlargement are expected to influence the number and distribution of local contact regions during subsequent paste-free Cu/Cu joining.

3.3. Mechanical and Metallographic Analysis

The bonding condition, mechanical response, and fracture behavior of the paste-free Cu/Cu joints were evaluated by optical microscopy, SEM, and adapted die-shear testing. Particular attention was paid to the distribution of local Cu/Cu contact regions, deformation of the laser-generated structures, remaining interfacial gaps, and material transfer after shear testing.

3.3.1. Bonding Surface Analysis

The bonded cross-sectional regions of structure variants I and II were examined by optical microscopy and SEM.

For structure variant I, shown in Figures 8 and 9, the interface was discontinuous and consisted mainly of isolated contact regions between the Cu matrix and the Cu substrate. The optical micrograph in Figure 8 shows a periodic sequence of locally connected regions along the interface. However, continuous contact was not established over the investigated cross-section.

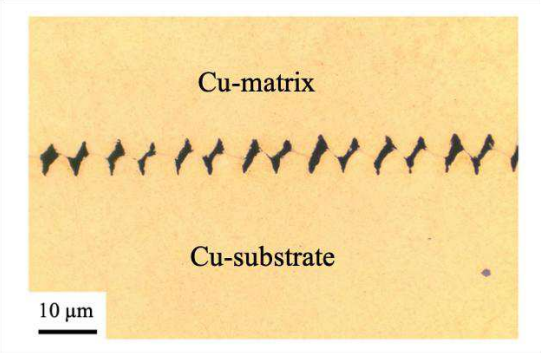


Fig.8 Optical micrograph of the bonded interface between the Cu matrix and Cu substrate for structure variant I.

The SEM images in Figure 9 confirm that local Cu/Cu contact was formed mainly at individual structure tips and side regions. Adjacent interfacial gaps and unbonded regions remained clearly visible. Even at higher magnification, parts of the original laser-generated geometry were still recognizable. This indicates that the structures were only locally deformed during joining and that continuous metallic contact was not established across the entire investigated interface.

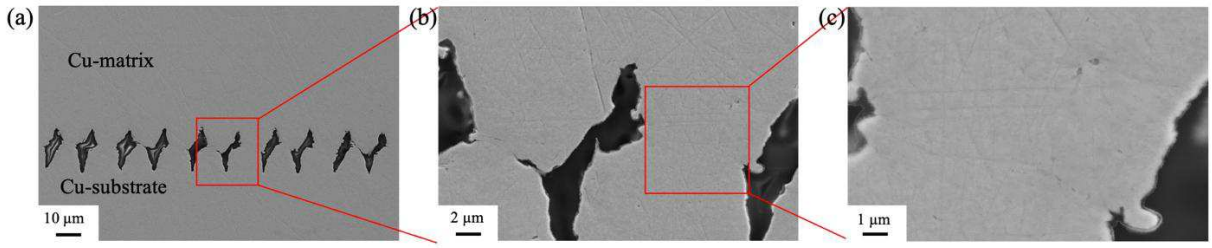


Fig.9 SEM images of the bonded interface for structure variant I at increasing magnifications: (a) overview of the interface; (b) intermediate magnification showing local Cu/Cu contact regions; and (c) higher magnification showing isolated contact zones and remaining interfacial gaps.

For structure variant II, shown in Figures 10 and 11, the interface exhibited a finer and more closely spaced morphology. The optical micrograph in Figure 10 shows a larger number of contact regions distributed along the interface. Compared with variant I, the distribution of connected regions appeared more continuous.

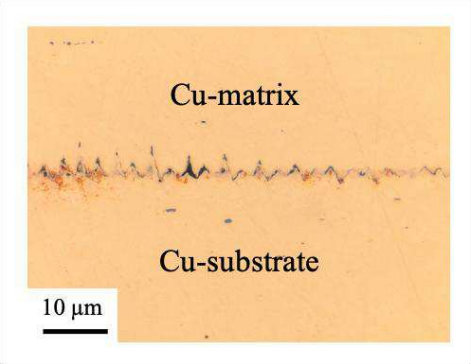


Fig.10 Optical micrograph of the bonded interface between the Cu matrix and Cu substrate for structure variant II.

The SEM images in Figure 11 show that the individual structures were more strongly deformed and adapted to the opposing copper surface. Local regions with continuous Cu/Cu contact were observed, while only smaller residual interfacial gaps remained. The original structure geometry was less clearly preserved than in variant I. The finer structural dimensions of variant II may have facilitated local deformation and geometrical adaptation between the opposing surfaces during joining.

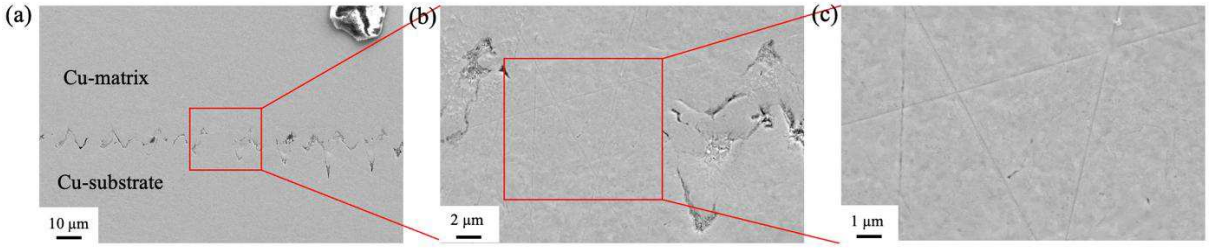


Fig.11 SEM images of the bonded interface for structure variant II at increasing magnifications: **(a)** overview of the interface; **(b)** intermediate magnification showing closely spaced Cu/Cu contact regions; and **(c)** higher magnification showing a finer and more continuously distributed interfacial contact morphology with smaller residual gaps.

Compared with variant I, structure variant II exhibited a more homogeneous interface with a larger number of closely spaced contact regions. Nevertheless, both variants still contained local interfacial discontinuities, indicating that complete bonding over the nominal joining area was not achieved.

The available optical and SEM observations do not allow a reliable determination of whether a thin intermediate layer, such as a residual copper oxide layer, remained within the locally bonded regions. Confirmation of such a layer would require additional chemical analysis or higher-resolution interfacial characterization.

3.3.2. Mechanical Analysis

The mechanical strength of the paste-free Cu/Cu joints was evaluated by adapted die-shear testing. The apparent shear strengths measured for structure variants I and II were approximately 16 and 35 MPa, respectively, as shown in Figure 12.

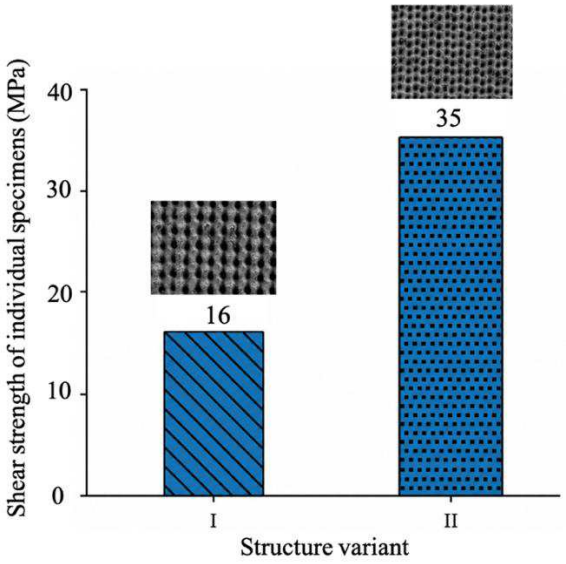


Fig.12 Apparent shear strength of the paste-free Cu/Cu joints produced using structure variants I and II. Each bar represents one measured specimen.

The value measured for structure variant II was more than twice that obtained for variant I. Since only one specimen was tested for each structure variant, the values represent individual measurements and should not be interpreted as a statistical comparison. Nevertheless, the results provide a preliminary indication of differences in the mechanical response of the two surface designs.

The mechanical results are consistent with the cross-sectional observations. Variant I exhibited mainly isolated contact regions and a discontinuous interface, whereas variant II showed a larger number of more closely spaced contact regions and a more continuous bonding morphology.

The difference in apparent shear strength appears to be associated primarily with the lateral morphology and density of the laser-generated surface structures rather than with areal roughness alone. Variant II exhibited a finer feature distribution and a higher surface-enlargement factor, which may have increased the number of effective local contact regions between the Cu matrix and Cu substrate.

The more densely distributed structures of variant II may also have promoted a more distributed transfer of mechanical load across the interface. In contrast, the larger and more widely spaced structures of variant I were associated with fewer local contact regions and a more discontinuous load-bearing interface.

Because only one specimen was tested for each structure variant, repeated mechanical testing is required to assess the reproducibility and statistical significance of the observed difference.

3.3.3. Fracture Surface Analysis

The fracture surfaces of the paste-free Cu/Cu joints were analyzed after shear testing and compared with the surface-topography data, cross-sectional observations, and apparent shear strengths of the two structure variants.

Figure 13 compares the surface morphologies of structure variants I and II before joining and after shear testing. The original laser-generated patterns remained recognizable for both variants. However, variant II exhibited a stronger modification of the initial surface morphology, including more pronounced deformation and material transfer.

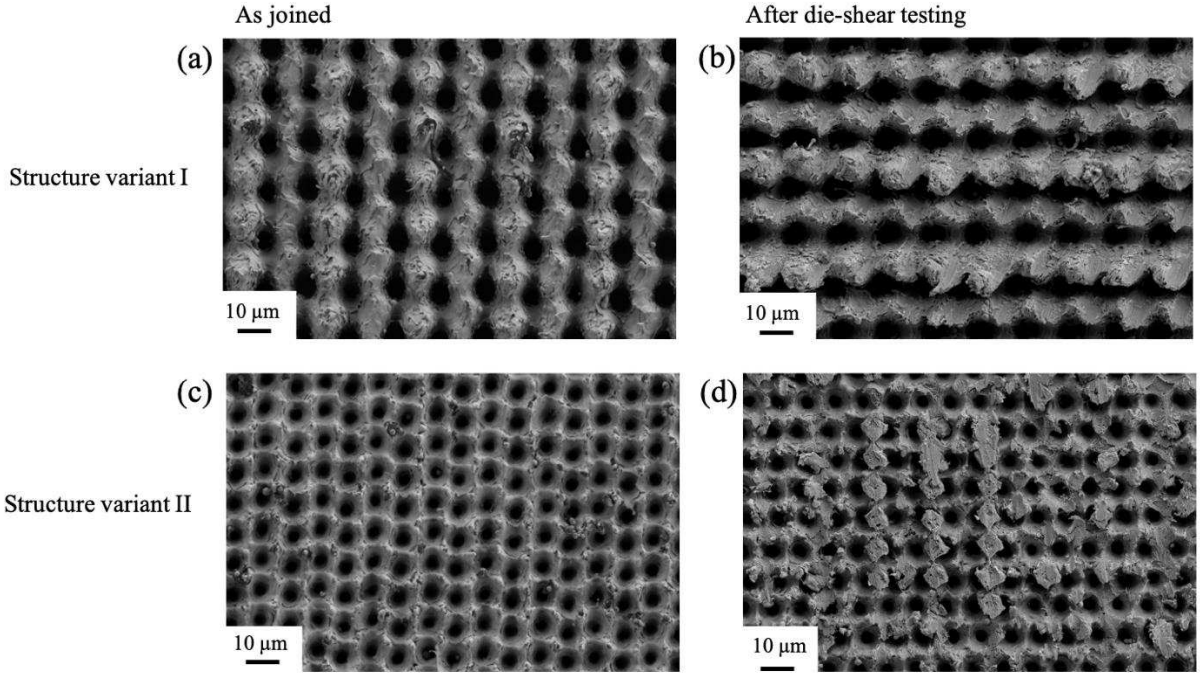


Fig.13 Comparison of the laser-structured copper surfaces before joining and after shear testing: (a) structure variant I before joining; (b) structure variant I after shear testing; (c) structure variant II before joining; and (d) structure variant II after shear testing.

The fracture-surface analysis of structure variant I is shown in Figure 14. Variant I exhibited areal roughness values of $Sa = 3.7 \pm 0.3$ µm and $Sz = 27.3 \pm 0.6$ µm, together with a surface-enlargement factor of 6.1 ± 1.3. The SEM images show local deformation, material transfer, and plastically affected regions. However, the original structural depressions remained clearly visible in several areas.

The coexistence of deformed and largely unchanged regions indicates heterogeneous joint formation. Local contact regions showed evidence of plastic interaction and material transfer, whereas larger areas remained only weakly bonded or unbonded. This observation is consistent with the cross-sectional analysis, in which contact was mainly found at isolated structure tips and side regions. The discontinuous bonding morphology is also consistent with the comparatively lower apparent shear strength of approximately 16 MPa.

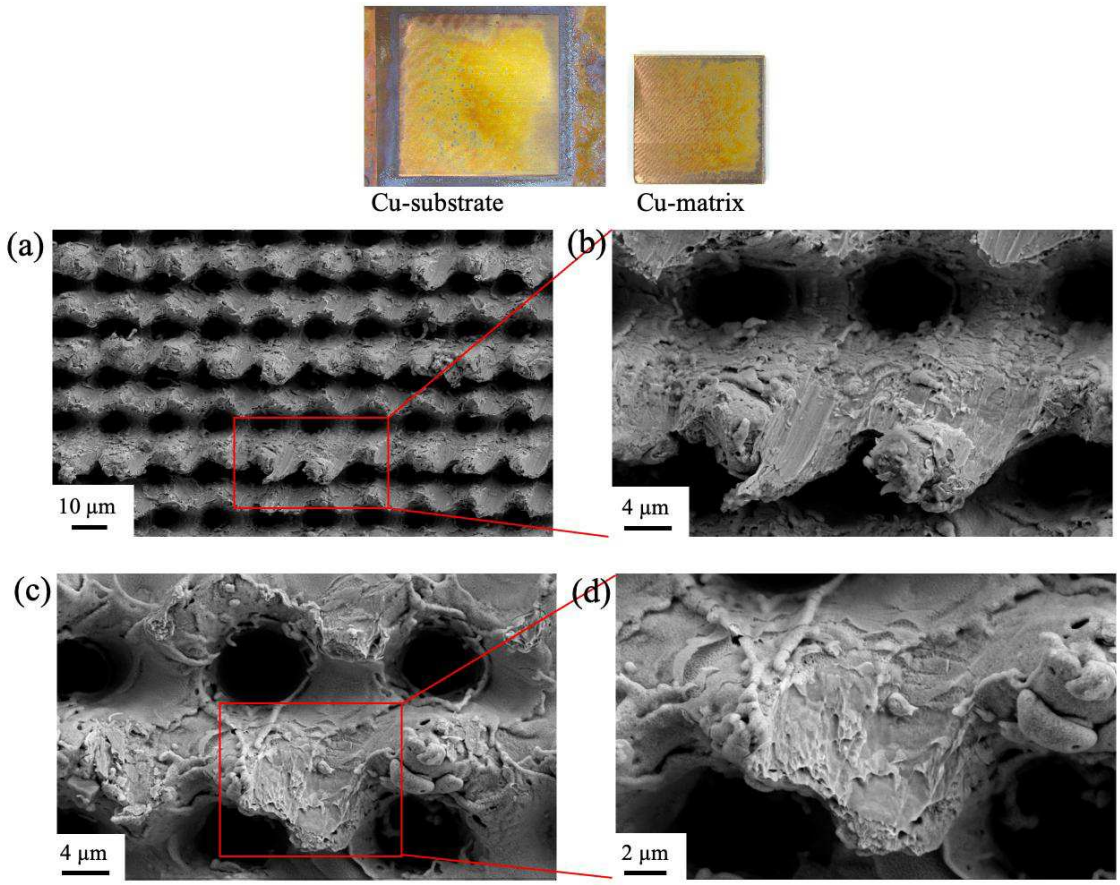


Fig.14 Fracture-surface analysis of structure variant I after shear testing: (a) overview of the fracture surface; (b) intermediate magnification showing local contact regions and material transfer; (c) higher magnification showing deformed structural elements; and (d) detailed view of incompletely bonded regions between adjacent structures.

The fracture-surface analysis of structure variant II is shown in Figure 15. Variant II exhibited lower areal roughness values of $Sa = 2.3 \pm 0.2$ µm and $Sz = 24.4 \pm 3.4$ µm, but a higher surface-enlargement factor of 8.0 ± 0.5. The fracture surface showed a stronger disturbance of the original morphology than variant I. Pronounced plastic deformation, material transfer, and partially torn structural elements were observed.

The finer and more densely distributed structures of variant II were associated with a larger number of locally affected regions across the fracture surface. This suggests that more individual contact regions may have contributed to load transfer during shear testing. The fracture morphology agrees with the cross-sectional observations, which revealed a more continuous distribution of bonded regions. This is also consistent with the higher apparent shear strength of approximately 35 MPa measured for variant II.

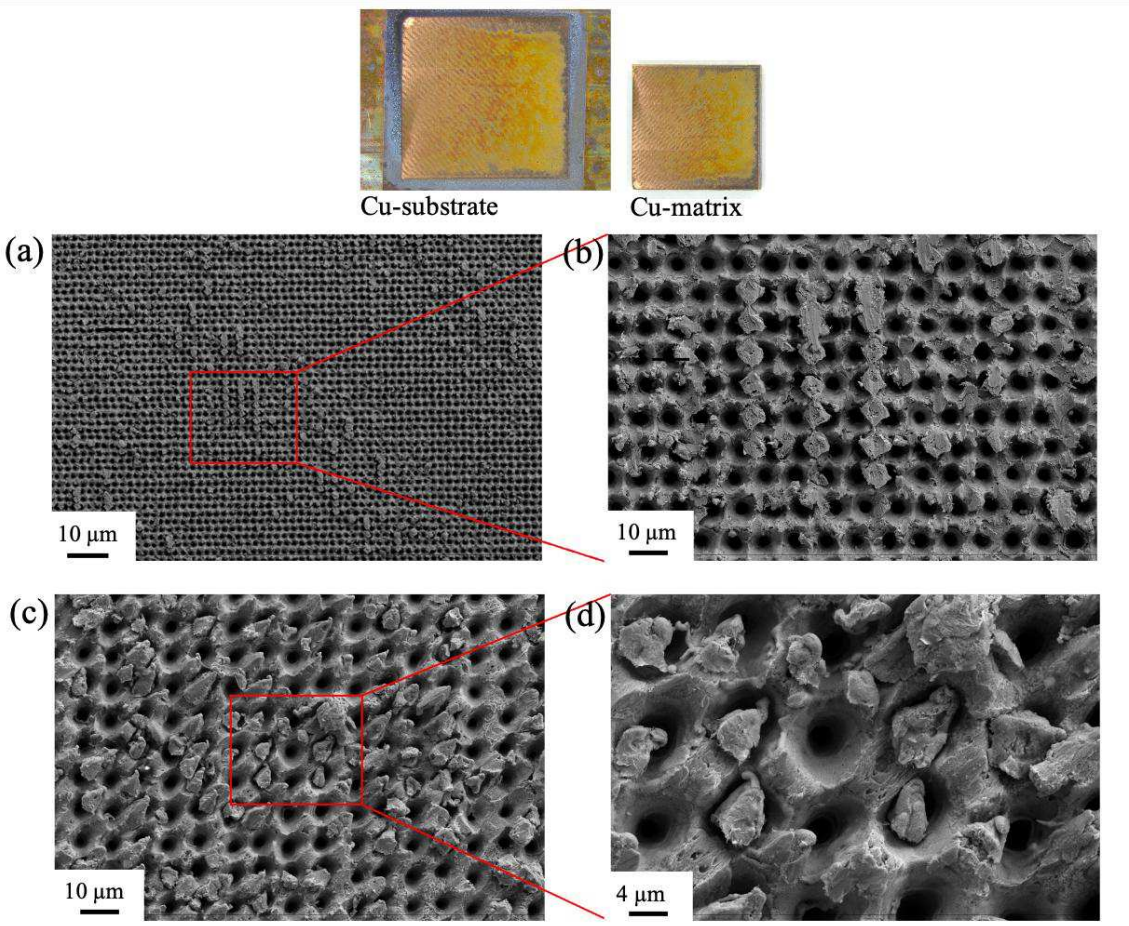


Fig.15 Fracture-surface analysis of structure variant II after shear testing: (a) overview of the fracture surface; (b) intermediate magnification showing densely distributed structural features and local material transfer; (c) higher magnification showing pronounced plastic deformation of the laser-generated structures; and (d) detailed view of strongly deformed and partially torn fracture regions.

The comparison indicates that the mechanical response cannot be attributed to areal roughness alone. Although variant II exhibited lower Sa and slightly lower Sz values than variant I, it showed a higher surface-enlargement factor, a finer lateral feature distribution, and a more continuous distribution of bonded regions. These characteristics may have increased the number of effective local contact regions and supported a more distributed load transfer across the joining interface.

Overall, variant I showed predominantly discontinuous bonding with remaining interfacial gaps between local contact zones. Variant II exhibited stronger plastic interaction, more extensive material transfer, and a more continuous bonding morphology. Nevertheless, the fracture surfaces indicate that both joints remained locally heterogeneous and that complete bonding over the nominal joining area was not achieved.

Taken together, the experimental results show that the laser-generated surface morphology had a clear influence on local Cu/Cu contact formation, interface continuity, and the measured mechanical response. In particular, the finer and more densely distributed structures of variant II were associated with a more continuous interfacial contact morphology and a higher apparent shear strength. These findings indicate that not only the roughness amplitude, but also the lateral scale, density, and surface enlargement of the laser-generated structures are relevant for paste-free Cu/Cu joint formation.

4. Conclusions

This study demonstrated the feasibility of paste-free direct Cu/Cu joining using two laser-structured copper surfaces.

With the help of kinematic simulations, the influence of the process parameters on the resulting surface roughness was analyzed. Depending on the pulse frequency (or energy), specific individual ablation geometries result. This means that a specific pulse/line spacing must be selected in each case to maximize surface roughness. While the surface structure could be predicted qualitatively with good agreement, adapted modeling will be required particularly for multiple passes over the surface in order to predict roughness values quantitatively with a better accuracy. The resulting and investigated variants exhibited distinct lateral morphologies and different surface-enlargement factors, while both showed pronounced micrometer-scale surface structures.

Initial shear-strength measurements showed promising results despite the microscale dimensions of the structures. The original assumption that nanoscale structures are needed, as known from other approaches as e.g., NanoWired technology, was not confirmed. In contrast, the results indicate that there could be a potential for thermomechanical joining in combination with laser microstructures. Further detailed analysis showed that the finer and more densely distributed features of variant II, together with its higher surface-enlargement factor, promoted a larger number of effective Cu/Cu contact regions.

The mechanical results should be regarded as preliminary because only one specimen was tested for each structure variant. Nevertheless, the combination of the shear-test results with the cross-sectional and fracture-surface observations indicates that the lateral scale, density, and distribution of the laser-generated structures are important for local contact formation and load transfer across the joining interface.

Overall, laser surface structuring represents a promising approach for paste-free direct Cu/Cu joining. Further work should focus on extended investigations of suitable surface structures, improving the homogeneity of the bonded interface, optimizing the joining parameters, and confirming the mechanical performance through repeated testing.

Acknowledgments:

The authors gratefully acknowledge MAHLE International GmbH, Stuttgart, Germany, for providing experimental facilities and technical support. The authors also thank the Institute of Materials Science and Engineering and the Institute for Machine Tools and Production Processes at Chemnitz University of Technology for their scientific support and assistance with surface structuring and characterization.

References

[1] Hou F, Sun Z, Su M, Fan J, You X, Li J, Wang Q, Cao L, Zhang G (2024) Review of die-attach materials for SiC high-temperature packaging. IEEE Trans Power Electron 39:13471–13486. https://doi.org/10.1109/TPEL.2024.3417529

[2] Wu N, Li Y (2025) A review of novel die attach materials for high-temperature WBG power electronic applications. Materials 18:3841. https://doi.org/10.3390/ma18163841

[3] Agirrezabala E, Aizpuru I, Garrido D, Portillo A (2025) Reliability of power semiconductor modules: a state-of-the-art review. IEEE Open J Power Electron 6:1036–1067. https://doi.org/10.1109/OJPEL.2025.3576994

[4] Liu S, Vuorinen V, Liu X, Fredrikson O, Brand S, Tiwary N, Lutz J, Paulasto-Kröckel M (2024) Fatigue crack networks in die-attach layers of IGBT modules under a power cycling test. IEEE Trans Power Electron 39:16695–16707. https://doi.org/10.1109/TPEL.2024.3447909

[5] Zhang C, Tuerpe M, Rabay B (2026) Considerations on joining technology of pressure-less sintering by nano-silver pastes. J Mater Eng Perform. https://doi.org/10.1007/s11665-026-13703-7

[6] Wakamoto K, Namazu T (2024) Mechanical characterization of sintered silver materials for power device packaging: a review. Energies 17:4105. https://doi.org/10.3390/en17164105

[7] Huo F, Chen C, Zhang Z, Lee S, Kim D, Zhang Y, Suetake A, Takeshita K, Yamaguchi Y, Momose Y, Suganuma K (2025) The impact of sintered Ag–Al interconnects on the power cycling reliability of die attachments. IEEE Trans Power Electron. https://doi.org/10.1109/TPEL.2025.3599973

[8] Yan H, Liang P, Mei Y, Feng Z (2020) Brief review of silver sinter-bonding processing for packaging high-temperature power devices. Chin J Electr Eng 6:25–34. https://doi.org/10.23919/CJEE.2020.000016

[9] Wang Y, Xu D, Yan H, Li C-F, Chen C, Li W (2024) Low-temperature copper sinter-joining technology for power electronics packaging: a review. J Mater Process Technol 332:118526. https://doi.org/10.1016/j.jmatprotec.2024.118526

[10] Wang X, Yang Z, Bian L, Liu W, Zhang G, Zhang J, Chen C, Liu P (2025) Copper-based composite sintering materials and reliability analysis for power electronics packaging. J Sci Adv Mater Devices 10:100963. https://doi.org/10.1016/j.jsamd.2025.100963

[11] Xin J, Gao Y, Zhang C, Yang L, Liu S, Li K, Zhou M, Liu Y, Zhang J, Cai W (2024) High performance Cu sintering joint for power devices enabled by in-situ generation of Cu particles with multi-level hierarchical structures. J Mater Process Technol 329:118435. https://doi.org/10.1016/j.jmatprotec.2024.118435

[12] Matsuda T, Yamada S, Okubo S, Hirose A (2023) Antioxidative copper sinter bonding under thermal aging utilizing reduction of cuprous oxide nanoparticles by polyethylene glycol. J Mater Sci 58:15617–15633. https://doi.org/10.1007/s10853-023-08976-5

[13] Helfers E, Müller FW, Schiebahn A, Reisgen U (2024) Influence of surface condition of copper sheets on ultrasonic metal welding. J Adv Join Process 9:100204. https://doi.org/10.1016/j.jajp.2024.100204

[14] Huang Y-C, Lin Y-X, Hsiung C-K, Hung T-H, Chen K-N (2023) Cu-based thermocompression bonding and Cu/dielectric hybrid bonding for three-dimensional integrated circuits applications. Nanomaterials 13:2490. https://doi.org/10.3390/nano13172490

[15] Lykova M, Panchenko I, Schneider-Ramelow M, Suga T, Mu F, Buschbeck R (2023) Cu–Cu thermocompression bonding with a self-assembled monolayer as oxidation protection for 3D/2.5D system integration. Micromachines 14:1365. https://doi.org/10.3390/mi14071365

[16] He C, Zhou J, Zhou R, Chen C, Jing S, Mu K, Huang Y-T, Chung C-C, Cherng S-J, Lu Y, Tu K-N, Feng S-P (2024) Nanocrystalline copper for direct copper-to-copper bonding with improved cross-interface formation at low thermal budget. Nat Commun 15:7095. https://doi.org/10.1038/s41467-024-51510-7

[17] Niu T, Xu K, Shen C, Sun T, Oberst J, Handwerker CA, Subbarayan G, Wang H, Zhang X (2023) In situ study on Cu-to-Cu thermal compression bonding. Crystals 13:989. https://doi.org/10.3390/cryst13070989

[18] Shimizu H, Nishikawa H, Hashimoto K (2025) Low-temperature Cu–Cu direct bonding enabled by a new method of plasma activation. J Vac Sci Technol B 43:052207. https://doi.org/10.1116/6.0004755

[19] Bickel S, Quednau S, Birlem O, Graff A, Altmann F, Junghähnel M, Panchenko J (2024) Fine-pitch copper nanowire interconnects for 2.5/3D system integration. J Electron Mater 53:4410–4420. https://doi.org/10.1007/s11664-024-11107-8

[20] Saborowski E, Steinert P, Lindner T, Schubert A, Lampke T (2023) Pin-shaped surface structures generated by laser single-pulse drilling for high-strength interfaces in thermally joined polymer–metal hybrids. Materials 16:687. https://doi.org/10.3390/ma16020687

[21] Zhang X, Wang R, Meng S, Chen W, Zhou L, He W, Pan X (2025) Advances and perspectives in laser texturing for adhesion enhancement: a comprehensive research progress. Prog Surf Sci 100:100781. https://doi.org/10.1016/j.progsurf.2025.100781

[22] Morello D, Leone C, Lamanna G, Genna S (2025) A two-step full laser surface treatment to improve the adhesive bonding of aluminium–aluminium joints. Int J Adhes Adhes 142:104089. https://doi.org/10.1016/j.ijadhadh.2025.104089

[23] Gaudiuso C, Fanelli F, Mezzapesa FP, Volpe A, Ancona A (2023) Tailoring the wettability of surface-textured copper using sub-THz bursts of femtosecond laser pulses. Appl Surf Sci 638:158032. https://doi.org/10.1016/j.apsusc.2023.158032

[24] Pöthig P, Grätzel M, Bergmann JP (2023) Influence of different surface conditions on mechanical properties during ultrasonic welding of aluminum wire strands and copper terminals. Weld World 67:1427–1436. https://doi.org/10.1007/s40194-023-01490-x

[25] Helfers E, Müller FW, Schiebahn A, Reisgen U (2026) Laser-based surface pretreatment for ultrasonic metal welding of copper and dissimilar aluminium–copper joints. Weld World 70:1051–1075. https://doi.org/10.1007/s40194-025-02197-x

[26] Yasa E, Kruth J-P (2010) Investigation of laser and process parameters for selective laser erosion. Precis Eng 34:101–112. https://doi.org/10.1016/j.precisioneng.2009.04.001

[27] Börner R, Winkler S, Junge T, Titsch C, Schubert A, Drossel W-G (2018) Generation of functional surfaces by using a simulation tool for surface prediction and micro structuring of cold-working steel with ultrasonic vibration assisted face milling. J Mater Process Technol 255:749–759. https://doi.org/10.1016/j.jmatprotec.2018.01.027

[28] Liu D, Li C, Dong L, Qin A, Zhang Y, Yang M, Gao T, Wang X, Liu M, Cui X, Ali HM, Sharma S (2024) Kinematics and improved surface roughness model in milling. Int J Adv Manuf Technol 131:2087–2108. https://doi.org/10.1007/s00170-022-10729-8

[29] Denkena B, Böß V, Nespor D, Samp A (2011) Kinematic and stochastic surface topography of machined TiAl6V4-parts by means of ball nose end milling. Procedia Eng 19:81–87. https://doi.org/10.1016/j.proeng.2011.11.083

[30] Wieland F, Gärtner E, Wieland S (2025) Structure and validation of a kinematic surface simulation model for the ultrashort-pulse direct-laser-writing process. Procedia CIRP 133:227–232. https://doi.org/10.1016/j.procir.2025.02.040

[31] Schaarschmidt I, Steinert P, Hackert-Oschätzchen M, Meichsner G, Zinecker M, Schubert A (2018) Simulation-based analysis of a microstructuring process for serrated surfaces with higher friction. In: Proceedings of the European COMSOL Conference, Lausanne, Switzerland. https://www.comsol.com/paper/64471

[32] DIN EN ISO 25178-2:2023-09 (2023) Geometrical product specifications (GPS)—surface texture: areal—Part 2: terms, definitions and surface texture parameters. DIN Media, Berlin. https://doi.org/10.31030/3294021

Statements and Declarations

Funding

This research received no external funding.

Competing Interests

C.Z. and M.T. were affiliated with MAHLE International GmbH during the conduct of this work. The authors declare no other competing interests.

Author Contributions

C.Z. performed the experimental work, data analysis, and manuscript preparation. P.S. contributed to the surface simulation and laser structuring. M.T. and A.S. supervised the work and contributed to the review and revision of the manuscript. All authors have read and agreed to the published version of the manuscript.

Data Availability Statement

The data presented in this study are available from the corresponding author upon reasonable request.